Electron Cascades in Sensors for Optical Detection of Ionizing Radiation

R. A. London, M. E. Lowry, S. P. Vernon, R. E. Stewart

Disclaimer

This document was prepared as an account of work sponsored by an agency of the United States government. Neither the United States government nor Lawrence Livermore National Security, LLC, nor any of their employees makes any warranty, expressed or implied, or assumes any legal liability or responsibility for the accuracy, completeness, or usefulness of any information, apparatus, product, or process disclosed, or represents that its use would not infringe privately owned rights. Reference herein to any specific commercial product, process, or service by trade name, trademark, manufacturer, or otherwise does not necessarily constitute or imply its endorsement, recommendation, or favoring by the United States government or Lawrence Livermore National Security, LLC. The views and opinions of authors expressed herein do not necessarily state or reflect those of the United States government or Lawrence Livermore National Security, LLC, and shall not be used for advertising or product endorsement purposes.

Electron Cascades in Sensors for Optical Detection of Ionizing Radiation

Richard A. London, Mark E. Lowry, Stephen P. Vernon, and Richard E. Stewart

Abstract

A new class of high-speed detectors, called RadOptic detectors, measures ionizing radiation incident on a transparent semiconductor by sensing changes in the refractive index with an optical probe beam. We describe the role of radiation-initiated electron cascades in setting the sensitivity and the spatial and temporal resolution of RadOptic detectors. We model electron cascades with both analytical and Monte Carlo computational methods. We find that the timescale for the development of an electron cascade is less than of order 100 fs and is not expected to affect the time response of a detector. The characteristic size of the electron cloud is typically less than 2 μm, enabling high spatial resolution in imaging systems. The electron-hole pair density created by single x-rays is much smaller than the saturation density and therefore single events should not saturate the detector.

I. INTRODUCTION

Conventional electronic radiation detectors collect the charge generated by the interaction of the radiation with a sensor medium, convert the charge to an electronic signal, and then transmit the signal to an electronic recording device. The processes of collection, amplification, and transmission smear the signal thereby limiting the temporal response of state-of-the-art electronic detection systems to tens of ps.

A new class of sensor, called RadOptic sensors, overcomes these limitations by using light to detect radiation ionization in place. Ionization of the sensor material, typically a II–VI or a III–V semiconductor alloy, produces a change in the optical refractive index that in turn produces a phase modulation of an optical probe beam (Lowry, et al. 2004, Vernon, et al. 2012). The recording of the probe beam provides the final step in the detection of the initial radiation. Since no net charge is produced and no charge transport is required, RadOptic sensors are inherently high-bandwidth, with the sensor temporal response determined by the charge carrier creation and relaxation times. We mention several other advantages that RadOptic sensors have over conventional detectors. 1) They do not suffer from space charge limitations on dynamic range. 2) The signal level depends upon the absorbed radiation fluence; thus shrinking the detector area does not reduce the signal level. This spatial scaling behavior can enable high-resolution imaging. 3) RadOptic systems can operate in very high radiation environments by using sensor materials insensitive to radiation damage and transmitting the output signals (i.e. coherent optical probe beams) to remote recorders. Single channel, multiple channel, and imaging detectors can be built using RadOptic sensors.

II. THE RADOPTIC EFFECT AND THE ROLE OF ELECTRON CASCADES

RadOptic sensors operate by detecting radiation-induced phase shifts. The phase shifts depend on changes in the index of refraction, $\delta n(r,t)$, which in turn depend on the density of electron-hole pairs, $\rho(r,t)$, created in the sensor material. As discussed in the Appendix, detection sensitivity, temporal resolution, and spatial resolution of the detection system ultimately depend on $\delta n(r,t)$ and therefore $\rho(r,t)$.

The time evolution of the RadOptic effect, namely the index change, $\delta n(r,t)$, can be divided into three stages: 1) charge generation, 2) cooling, and 3) dissipation. Charge generation is dominated by electron cascade and collisional processes for particle energies above 10 eV. Cooling takes the charges from energies of approximately 10 eV to energies just above the bandgap. Dissipation is controlled by charge diffusion and recombination. Since δn is dominated by the population of charge states near the bandgap, the generation and cooling processes determine the rise time of the RadOptic effect. Dissipation processes influence detection sensitivity, sensor fall-time and sensor recovery. It is important to determine the characteristic times for these processes. Cooling timescales range from a few hundred fs to a few ps (Gong 1990, Zhou 1990, Hohenester 1993), while dissipation occurs on timescales ranging from 100 ps to a several ns (Weiner, 1984). The charge generation process and associated timescales are a major focus of this paper.

The spatial distribution of the pair density is important in determining the sensitivity and saturation of a sensor. The refractive index is generally proportional to $\rho(r,t)$ at low pair density and saturates at high pair density, of order 10^{18} cm^{-3} in GaAs (Park, 1988). A quantitative discussion of the phase shift and saturation effects experienced by an optical beam probing a sensor region exposed to x-rays is presented in the Appendix. Therein it is shown that the phase shift is due to the additive effect of a large number of phase objects, each created by the absorption of a single x-ray. In the low x-ray fluence regime, these phase objects remain separated, while at high fluence they overlap. It is important to determine the value of the local charge density due to single events compared to the index saturation value to quantify the sensitivity and linearity of a RadOptic detector.

In addition, the spatial dependence of the charge distribution is important for imaging sensors using the RadOptic effect to record the phase replica of an x-ray image (Baker 2012, Vernon 2012, Stewart 2013). The size of the electron-hole cloud produced by a primary photoelectron from a high-energy x-ray limits the spatial resolution of the replica pattern.

We now discuss the underlying physical mechanisms of the generation of electron-hole pairs in RadOptic sensors. Each energetic charged particle or photon that strikes a semiconductor material generates a large number of ionizations and thereby electron-hole pairs, which we call "charges" for short. This occurs through an ionization cascade process. For x-rays, the cascade begins with the ionization of an atom, creating a photoelectron, followed by either a fluorescent photon or one, or several, Auger electrons. Fluorescent photons are often reabsorbed, creating further photo and Auger

electrons. The photo and Auger electrons then slow down, primarily by collisional ionization, creating "secondary electrons" that in turn can generate more charges. This cascade process continues until the charges either leave the material or scatter down to sufficiently low energy that that they can no longer ionize the material. It is well known that the final number of charges N_e created before recombination is proportional to the energy of the incident particle, E_x: $N_e = E_x/\varepsilon$, where the constant ε is known as the pair-creation energy. For semiconductors and insulators, ε is typically 2-3 times the bandgap energy (Klein, 1968). Bertuccio (2002) have found a value of $\varepsilon = 4.18$ eV for GaAs. The result of the electron cascade is the production of a certain number of final charges for each incident particle or x-ray. At this point, the RadOptic optical probe senses the charge density. The electrons then recombine with the holes, generally on a longer timescale than the cascade or detection process.

We are motivated to study the space and time dependence of electron cascades created by single particles. Previous work has considered cascades in diamond applied to problems of material damage from high intensity short pulse x-ray sources (Ziaja, 2005). Here we consider similar cascades in gallium arsenide, a prime candidate material for RadOptic sensors. Since the interaction of x-rays with the sensor material is dominated by photo-ionization (elastic and inelastic scattering cross-sections are 10^{-2} to 10^{-3} times smaller), and photo-ionization produces electrons with energies somewhat less than the x-ray energy, we consider the cascades resulting from electrons in the 5-40 keV energy range. This broad range is important for applications such as detection of x-rays produced by laser generated back lighters (Blue, 2005, Kalantar, 2005), x-ray emission from capsule implosions in inertial confinement fusion (Kyrala, 2010), and fast secondary electron detection for neutron and gamma ray converters to detect fusion reaction products (Malone, 2010).

III. ANALYTIC MODEL FOR ELECTRON CASCADE TIME RESPONSE.

The time scale for the full development of an electron cascade can be estimated from the energy dependent stopping power, $S(E)$, defined as the average energy loss per unit length of travel of a particle in matter, usually expressed in units of eV/Å. The approximation of equating the electron cascade time to the slowing down time assumes that the primary electron loses energy in many steps, with each step involving a relatively small energy loss by creating secondary electrons. This is usually valid, since we are considering electron energies of order 10 keV, whereas the characteristic energy transfer per collision is of order the binding energy of electrons, which is approximately 10 eV. The secondary electrons are assumed to create further ionizations and lose their energy essentially instantaneously. Thus, the cascade time is calculated as the slowing down time of the primary electron. Given $S(E)$, we calculate the slowing down time as:

$$t_s = \int_{E_f}^{E_i} \left[\frac{1}{v(E)S(E)} \right] dE,$$

where E_i and E_f are the initial and final energies of the electron and v is the electron

3

velocity as it slows down. We use data for electron slowing down in GaAs for energies between 10 eV and 10 keV from Joy (1995). We add data for $10 < E \leq 30$ keV by scaling the values for Ge given by Powell (2012) by the ratio of the 10 keV stopping power for GaAs to that for Ge. The calculated time to slow down to 10 eV from various initial energies in GaAs is shown in Figure 1. We see that the slowing down time increases rapidly with initial electron energy. This justifies the use of the slowing-down time to calculate the cascade time, since secondary electrons, being of lower energy, slow down much faster than primary electrons. The slowing down time ranges from 3 fs for 1 keV electrons up to 70 fs for 30 keV electrons. In all cases of interest the slowing down time is less than 100 fs.

IV. MONTE CARLO CALCULATIONS OF ELECTRON CASCADES.

In order to obtain more accurate calculations of the electron cascade time and to address the spatial distribution of charge density, we have performed Monte Carlo calculations using the MCNP code (http://mcnp.lanl.gov). This is a general-purpose code for simulating the transport of high-energy radiation within cold matter. The treatment of electron transport is described in several publications (Hughes, 1996 and 2013). It includes processes of atomic excitation and ionization, elastic scattering and bremsstrahlung. Electrons at higher energies (> 1 keV) are treated with the condensed history method (Berger, 1963), while lower energy electrons are treated with the single-event method. Recent enhancements in the methods and cross section data provide good accuracy for electrons of energies as low as 10 eV.

A. Problem geometry

We examine cascades initiated by electrons created inside the sensor material by photo- and/or Auger ionization. The problem geometry is illustrated in Figure 2. We assume a cylinder of material large enough that no electrons escape. The electrons are launched in the +z direction at middle of the cylinder (r=0, z=0). A large number (10^5 to 10^6) of electrons are launched, each with a different random number seeds in order to produce average distributions. We then tabulate the space and time dependent energy deposition in specified bins.

B. Spatial dependence

Figure 3 shows the spatial distribution of the final energy deposition in 0.05 by 0.05 μm spatial bins for electrons of 20-keV initial energy. We see a sharply peaked distribution of dose about the position of the initial electron. The peak value of the dose is not physically meaningful, since the dose distribution is singular due to the specification of an infinitesimally small beam width. The results of the Monte Carlo calculations are therefore dependent on the spatial bin size. This anomaly at the source point can be avoided by considering cumulative doses moving out from the source.

Figure 4 shows lineouts of the cumulative dose in r and z. The cumulative dose in r is defined as the integral over all z and over r less than the specified value. A similar

4

definition applies to the cumulative dose in z. For this case of 20 keV initial electrons, 75% of the energy is deposited in the forward direction (i.e. for z>0), with the rest deposited in the backward direction (z <0). Half of the forward deposition occurs for z < 0.46 μm, while 1/2 of the backward deposition occurs for z > -0.30 μm. In the radial direction 1/2 of the energy is deposited for r < 0.67 μm. This results in a characteristic volume for the energy deposition of 1.1 μm^3.

In order to obtain realistic results for the electron density, we must consider the physics of low energy electrons. This is beyond the scope of MCNP, which does not follow electrons below 10 eV. When an electron drops below this energy, or a process creates such a low energy electron, it is assumed to stop immediately, depositing its energy locally. In reality, most of the electrons generated by an absorbed x-ray drop to such low energies very quickly and these low energy electrons are responsible for the refractive index change that is essential to the operation of the detector. Therefore, we calculate the electron density from the energy deposition using the pair creation energy (ε=4.18 eV) discussed above. An addition, we are only interested in the charge density due to a single primary electron at a time corresponding to the minimum feasible detector time resolution, of order 1 ps (Lowry, 2011, Bennett, 2011). The low energy electrons (and holes) will travel some distance in this time. Since collisions with the lattice are rapid, these electrons will move diffusively. Therefore, we consider the diffusion of charge between the initial cascade time modeled by the MCNP code (~ 50-100 fs) and the time corresponding to the detector resolution (~ 1 ps). Considering a point source, the diffusion length, or average distance an electron will move is: $\langle x \rangle = \sqrt{(Dt)}$, where D is the diffusivity and t is the time. Taking the room temperature mobility given by Beard et al. (2000) and the Einstein relation between diffusivity and mobility: $D = \mu kT/e$, we find D=0.0169 μm^2/ps. Therefore the diffusion length is $\langle x \rangle = 0.13$ μm $t_{ps}^{1/2}$, where t_{ps} is time in ps. To get the electron density at a specific time, we first calculate the energy deposition with MCNP on a fine grid, convert this to electron density and then smooth the density over the diffusion length. This produces the electron density map at 1 ps shown in Figure 5. The peak density is 2.1×10^{16} cm^{-3}, and the size of the region where the density drops to 10% of the peak value is Δr=0.3 by Δz=0.5 μm.

Monte Carlo calculations have been performed for primary electron energies ranging from 5 to 40 keV. Results for the peak electron density and the positions containing ½ of the electrons in –z, +z and r directions are shown in Figure 6. The peak density decreases monotonically with increasing initial energy, from 1.2×10^{17}cm^{-3} at 5 keV to 10^{16} cm^{-3} at 40 keV, while the lengths characterizing ½ of the electron number increase monotonically with energy. In other words, the higher energy electrons deposit their energy over larger volumes and these volumes increase faster than the energy, so that the electron density/particle decreases with energy. In all cases the peak electron density is less than the expected saturation density of 10^{18} cm^{-3}. In this case, Eq. A9 in the Appendix shows that the sensitivity parameter, κ, is independent of the radiation induced charge density. Therefore we do not expect that single particle events will cause local saturation.

C. Time dependence

The time dependence of the development of the electron cascades has also been calculated in the Monte Carlo simulations. Figure 6 shows the charge generation rate versus time for incident electron energies ranging from 5 to 40 keV. In all cases, we see a gradual rise in the generation rate to a maximum value, followed by a rapid drop until all of the incident energy has been converted to charge. The initial rise is due to the increase in inelastic cross section with decreasing energy of the primary electron. Figure 8 shows the time for generating 90% of the final charge versus initial electron energy, together with the slowing down time presented in section 2. We note that the cascade generation time grows somewhat faster than linearly with primary energy. The Monte Carlo results agree with the analytical estimate to within 20%. For energies less than 40 keV, the generation time is less than 120 fs. The Monte Carlo results thus support the conclusions drawn above that the time to generate the charge responsible for the RadOptic effect is generally less than 100 fs and will therefore enable time resolutions of this order.

V. CONCLUSIONS.

We have described the role of radiation initiated electron cascades in the operation of a new class of optically probed radiation "RadOptic" detectors. The space and time dependence of the electron cascades influence the sensitivity and the space and time resolution of such detectors. An analytical model predicts cascade time scales between 1 and 70 fs for electrons of energies between 0.1 and 30 keV in GaAs. Detailed Monte Carlo simulations give similar timescales (within 20%) and extend the analytical results to 120 fs at 40 keV. The Monte Carlo simulations predict characteristic spatial extents of the charge clouds created by electrons between 5 and 40 keV of 0.1 to 2.3 μm and charge densities ranging from 11 to 1 x 10^{16} cm^{-3}. The timescales for the development of the electron cascades, less than of order 100 fs, are generally less than the other times scales of the RadOptic process, namely the charge cooling timescale and the diffusion and recombination timescales. Thus that the cascade process is fast and it is not expected affect the time response of RadOptic detectors. The spatial scale of the electron clouds is small enough that it should allow better than 5-μm resolution in imaging applications. The electron-hole pair densities created by single x-rays are much smaller than the saturation density and therefore single events should not saturate the detectors.

REFERENCES

Baker, K. L., Stewart, R. E., Steele, P. T., Vernon, S. P., and Hsing, W. W. "Ultrafast semiconductor x-ray detector", Appl. Phys. Lett., **101**, 031107-1-3 (2012).

Banyai, L., and Koch, S. W., "A Simple Theory for the Effects of Plasma Screening on the Optical Spectra of Highly Excited Semiconductors", Z. Phys. B, **63**, 283-291 (1986).

Beard, M. C., Turner, G. M., and Schmuttenmaer, C. A., "Subpicosecond carrier dynamics in low-temperature grown GaAs as measured by time-resolved terahertz spectroscopy," J. Appl. Phys., **90**, 5915-5923 (2001).

Bennett, C.V., Hernandez, V. J., Moran, B. D., Lowry, M.E., Vernon, S.P., Steele, P.T., Chang, D., and Fejer, M. M. "Time Lens Based Single-Shot Ultrafast Waveform Recording: From High Repetition Rate to High Dynamic Range," pp. 223-224, Proc. Ultrafast Optics 2011. Monterey, CA, (2011).

Berger, M. J., "Monte Carlo Calculation of the Penetration and Diffusion of Fast Charged Particles" in Methods in Computational Physics, Vol. 1, ed. B. Alder, S. Fernbach, and M. Rotenberg (Academic Press, NY, 1963), p. 135.

Bertuccio G., and Maiocchi, D., "Electron-hole pair generation energy in gallium-arsenide by x and γ photons," J. Appl. Phys. **92**, 1248-1255 (2002).

Blue, B. E., Weber, S. V., Glendinning, S. G., Lanier, N. E., Woods, D. T., Bono, M. J., Dixit, S. N., Haynam, C. A., Holder, J. P., Kalantar, D. H., MacGowan, B. J., Nikitin, A. J., Rekow, V. V., Van Wonterghem, B. M., Moses, E. I., Stry, P. E., Wilde, B. H., Hsing, W. W., and Robey, H. F., "Experimental Investigation of High-Mach-Number 3D Hydrodynamic Jets at the National Ignition Facility," Phys. Rev. Lett. **94**, 095005-1-4 (2005).

Gong, T., Nighan, Jr., W. L., and Fauchet, P. M., "Hot Carrier Coulomb Effects In GaAs Investigated By Femtosecond Spectroscopy Around The Band Edge," Appl. Phys. Lett. **57**, 2713-2715 (1990).

Hohenester, U., Supancic, P., Kocevar, P., Zhou, X. Q. , Kutt, W., and Kurz, H. "Subpicosecond thermalization and relaxation of highly photoexcited electrons and holes in intrinsic and p-type GaAs and InP" , Phys. Rev. B , **47**, 13-233-245 (1993).

Hughes, H. G., "Treating Electron Transport in MCNP" Los Alamos National Laboratory, Report LA-UR-96-4583, available at http://mcnp.lanl.gov(1995).

Hughes, H. G. "Recent Developments in Low-Energy Electron/Photon Transport for MCNP6" submitted to Prog. Nuc. Sci. Tech., available at http://mcnp.lanl.gov (2013).

Hyatt M. Gibbs, *Bistability: Controlling Light with Light*, Academic Press, Orlando (1985), p. 137.

Joy, D. C., "A Database on Electron-Solid Interactions," Scanning, **17**, 270-275 (1995).

Kalantar, D. H. and Belak, J. F. and Collins, G. W. and Colvin, J. D. and Davies, H. M. and Eggert, J. H. and Germann, T. C. and Hawreliak, J. and Holian, B. L. and Kadau, K. and Lomdahl, P. S. and Lorenzana, H. E. and Meyers, M. A. and Rosolankova, K. and Schneider, M. S. and Sheppard, J. and Stolken, J. S. and Wark, J. S., "Direct Observation of the α−ε Transition in Shock-Compressed Iron via Nanosecond X-Ray Diffraction," Phys. Rev. Lett. **95**, 075502-1-4 (2005).

Klein, C. A., "Bandgap Dependence and Related Features of Radiation Ionization Energies in Semiconductors," J. Appl. Phys. **39**, 2029-2038 (1968).

Kyrala, G. A., Dixit, S., Glenzer, S., Kalantar, D., Bradley, D., Izumi, N., Meezan, N., Landen, O. L., Callahan, D., Weber, S. V., Holder, J. P., Glenn, S., Edwards, M. J., Bell, P., Kimbrough, J., Koch, J., Prasad, R., Suter, L., Kline, J. L., Kilkenny, J., "Measuring symmetry of implosions in cryogenic hohlraums at the NIF using gated x-ray detectors," Rev. Sci. Instrum., **81**, 10E316-1-10 (2010)

Lee, Y. H., Chavez-Pirson, A., Koch, S. W., Gibbs, H. M., Park, S. H., Morhange, J., Jeffery, A., Peyghambarian, N., Banyai, L., Gossard, A. C., Wiegmann, W., "Room-Temperature Optical Nonlinearities in GaAs", Phys. Rev. Lett. **57**, 2446-2449 (1986).

Lowry, M. E., Bennett, C. V., Vernon, S. P., Bond, T., Welty, R., Behymer, E., Peterson, H., Krey, A., Stewart, R., Kobayashi, N. P., Sperry, V., Stephan, P., Reinhardt, C., Simpson, S., Stratton, P., Bionta, R., McKernan, M., Ables, E., Ott, L., Bond, S., Ayers, J., Landen, O. L., and Bell, P. M., "RadSensor: X-Ray Detection by Direct Modulation of an Optical Probe Beam," in Fourth-Generation X-Ray Sources and Ultrafast X-Ray Detectors, Ed.: R. O. Tatchyn, Z. Chang, J.-C. Kieffer, and J. B. Hastings, Proc. of SPIE, **5194**, 2004, p. 193-204.

Lowry, M. E. Vernon, S. P., Steele, P. T., Bennett, C. V., Hernandez, V. J., Moran, B., and Haynes, S. "Radoptic x-ray detection with picosecond resolution", Proc. 8th Int. Conf. on Ultrafast Optics, 2011.

Malone, R. M., Cox, B. C., Frogget, B. C., Kaufman, M. I., Tibbitts, A., Tunnell, T. W., Evans, S. C., Herrmann, H. W., Kim, Y. H., Mack, J. M., Young, C. S., McGillivray, K. D., Palagi, M. J., and Stoeffl, W., "Overview of the Gamma Reaction History Diagnostic for the National Ignition Facility (NIF)," in SPIE-OSA, **7652,** 76520Z-10 (2010).

Park, S.H., Morhange, J.F., Jeffery, A.D., Morgan, R.A., Chavez-Pirson, A., Gibbs, H.M., Koch, S.W., Peyghambarian, N., Derstine, M., Gossard, A.C., English, J.H., Weigmann, W., "Measurements of room-temperature band-gap-resonant optical nonlinearities of GaAs/AlGaAs multiple quantum wells and bulk GaAs," Appl. Phys. Lett., **52**, 1201-1203 (1988).

Powell, C. J., "Electron Stopping Powers," in CRC Handbook of Chemistry and Physics, 92nd Edition (Internet Version 2012), W. M. Haynes, ed., CRC Press/Taylor and Francis, Boca Raton, FL.

Said, A. A., Sheik-Bahae, M., Hagan, D. J., Wei, T. H., Wang, J., Young, J., and Van Stryland, E. W., "Determination of bound-electronic and free-carrier nonlinearities in ZnSe, GaAs, CdTe, and ZnTe," J. Opt. Soc. Am. B **9**, 405-414 (1992).

Stewart, R. E., Steele, P. T., Baker, K. L., Vernon, S. P., and Hsing, W. W., "Transient-Grating Framing Camera with 1 ps Resolution," submitted (2013).

Vernon, S. P., Lowry, M. E., Baker, K. L., Bennett, C. V., Celeste, J. R., Cerjan, C., Haynes, S., Hernandez, V. J., Hsing, W. W., LaCaille, G. A., London, R. A., Moran, B., Schach von Wittenau, A., Steele, P. T., and Stewart, R. E., "X-ray bang-time and fusion reaction history at picosecond resolution using RadOptic detection," Rev. Sci. Inst. **83**, 10D307-1-3 (2012).

Weiner, J. S. and Yu, P. Y., "Free carrier lifetime in semi-insulating GaAs from time resolved band to band photoluminescence", J. Appl. Phys. **55**, 3889-3891 (1984).

Ziaja, B, London, R. A., and Hajdu, J., "Unified model of secondary electron cascades in diamond," J. Appl. Phys., **97**, 064905-1-9 (2005).

Zhou, X. Q., Lemmer, U., Seibert, K., Cho, G.C., Kutt, W. , Walter, K., and Kurz, H., "Subpicosecond Dynamics of Hot Carrier Relaxation in InP and GaAs", in Applications of Ultrashort Laser Pulses in Science and Technology, Proc. SPIE **1268**, 1990, p.166-176.

APPENDIX: PHYSICS AND SATURATION OF THE RADOPTIC EFFECT

The RadOptic effect relies upon a change in the refractive index similar to the optical nonlinearity described by Lee (1986) and Park (1988). In this phenomenon an optical pump beam creates electron-hole pairs, which change the refractive index seen by a probe beam. A thorough treatment of the optical index change in excited semiconductors is given by Banyai and Koch (1986). We utilize a simpler, yet sufficiently accurate treatment for our application. At low densities, the free electron contribution to the optical nonlinearity is proportional to the pair density (Said 1992). To account for high-density effects, we adopt the saturation expression of Park and Gibbs (1985) to modify Said's formula and write the index change as:

$$(A1) \quad \delta n = \rho \sigma(\lambda) f(\rho),$$

where ρ is the electron-hole pair density, λ is the wavelength of the probe, and $\sigma(\lambda)$ is the low-density index change coefficient, which varies slowly with λ except very close to the bandgap. Typically $\sigma(\lambda)$ is negative. The saturation function is written as:

$$(A2) \quad f(\rho) = \frac{1}{1 + \rho / \rho_{sat}},$$

where $\rho_{sat} \sim 10^{18}$ cm^{-3}.

If the pair density is uniform throughout the volume interrogated by the probe beam, the single-pass phase shift is given by:

$$(A3) \quad \Delta\phi = \frac{2\pi S}{\lambda} \delta n,$$

where S is the path length of the probe.

In the case of incident x-rays, the index change is generally thought to be non-uniform, since each x-ray creates a small volume of ionization localized around the point where it is absorbed. Thus the net effect can be viewed as an ensemble of phase objects, as illustrated in Figure A1. At high fluence the phase objects overlap, producing a fairly uniform index change, and the phase shift is given by Eqs. (A1-A3), where ρ is averaged over the probed region.

At low incident fluence, the phase objects remain largely separated and the total phase shift is given by the additive effects of the many phase objects in the region probed by the optical beam. In this limit we express the phase change as a linear superposition:

$$(A4) \quad \Delta\phi = N_x \delta\phi,$$

where N_x is the number of x-ray generated phase objects, and $\delta\phi$ is the phase shift induced by a single object:

$$(A5) \quad \delta\phi = \frac{2\pi s}{\lambda} \langle \delta n \rangle.$$

Here the index change averaged over the area of the optical probe beam, A, is approximated by

$$(A6) \quad \langle \delta n \rangle = \frac{s^2}{A} \delta n \ .$$

We have assumed a cubic excitation volume of edge length s, and δn is the index change within this volume. Then the object phase shift is

$$(A7) \quad \delta\phi = \frac{2\pi}{\lambda}\frac{s^3}{A}\delta n \ .$$

We see that the radiation induced object phase shift is proportional to the volume of the object, s^3, as well as the index change within the object, δn. If we further assume that δn can be described by the same formalism used in nonlinear optics, we can write:

$$(A6) \quad \delta\phi = \frac{2\pi}{\lambda}\frac{s^3}{A}\rho_{po}\ \sigma(\lambda)f\left(\rho_{po}\right),$$

where $\rho_{po} = N_{eh}/s^3$ is the density of e-h pairs within the phase object and $N_{eh} =$ number of e-h pairs produced per absorbed x-ray. Since the number of pairs is proportional to the x-ray photon energy, $N_{eh}=E_x/\varepsilon$ (Section 1), we can write the object phase shift as:

$$(A7) \quad \delta\phi = \frac{2\pi}{\lambda}\frac{E_x}{\varepsilon A}\ \sigma(\lambda)f\left(\rho_{po}\right).$$

Finally we arrive at an expression for the phase shift due to the whole radiation pulse absorbed in the sensor that holds when the phase objects do not overlap and/or the density in each object remains much smaller than the saturation density ($\rho_{po} \ll \rho_{sat}$). In this case we get the total phase shift by multiplying $\delta\phi$ by the number of phase objects:

$$(A8) \quad \Delta\phi = \kappa\ F_x \ ,$$

where κ is a sensitivity parameter:

$$(A9) \quad \kappa = \frac{2\pi}{\lambda\varepsilon}\sigma(\lambda)f\left(\rho_{po}\right),$$

and $F_x = N_x E_x/A$ is the absorbed x-ray energy fluence within the probe beam.

We note that κ depends on ε and the probe wavelength and has a saturation function determined by the pair density in each phase object. Further, we see that the phase signal depends upon the absorbed fluence; this behavior is very different from conventional detectors in that shrinking the detector size does not impact the signal level.
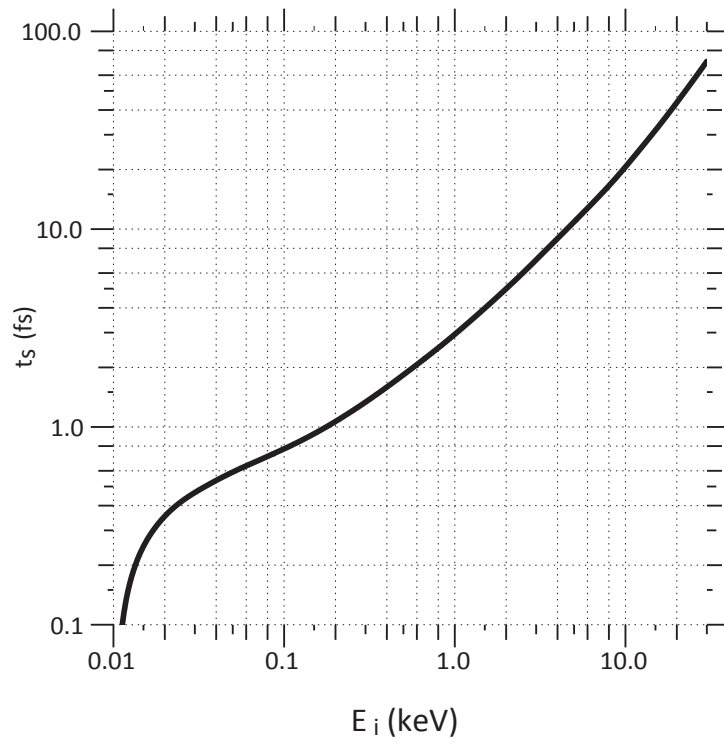
FIGURES

Figure 1. Time to slow down to 10 eV in GaAs versus initial electron energy E_i.
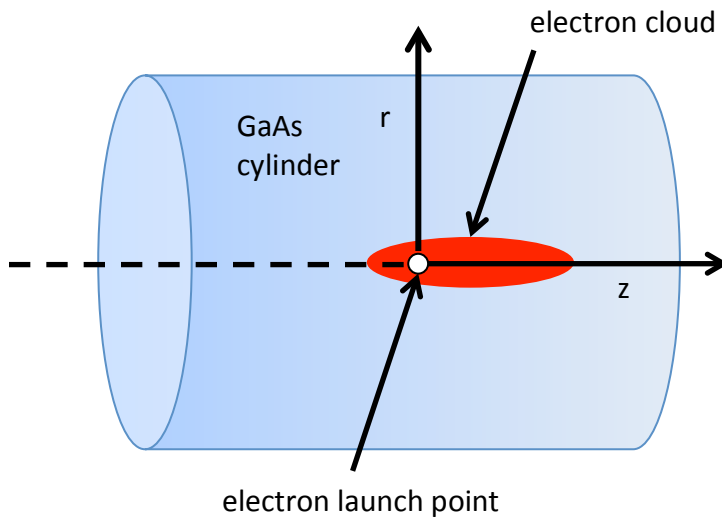

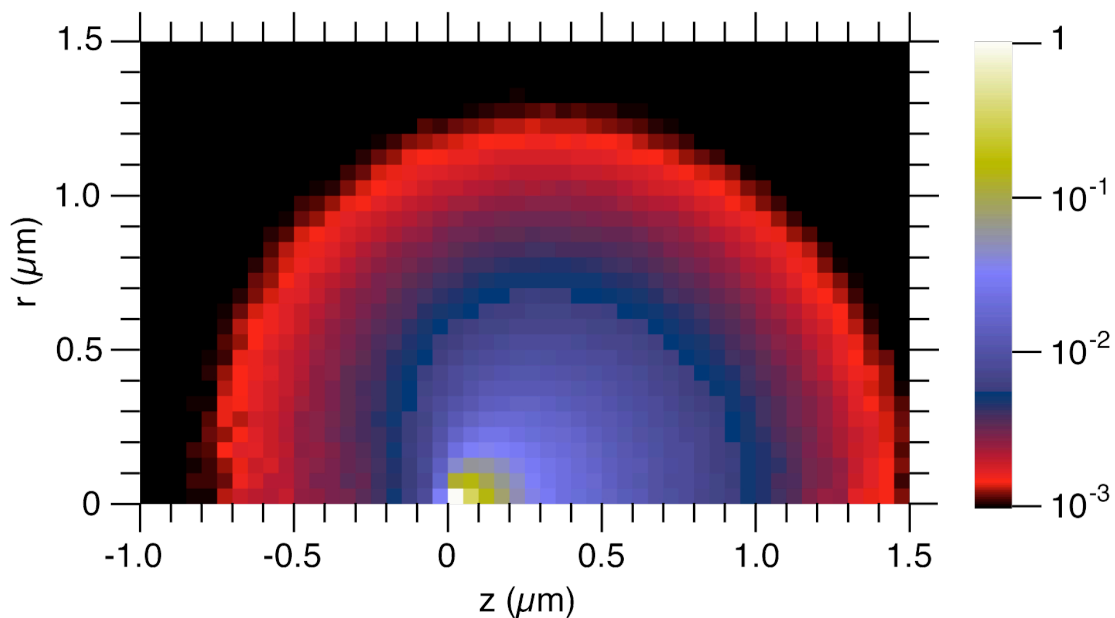Figure 2. Geometry for Monte Carlo calculations.

Figure 3. Energy deposition per unit mass (dose) for 20 keV electrons in GaAs. The color scale is logarithmic as indicated on the right side, with the values scaled to the maximum deposition of 10^{11} MeV/g.
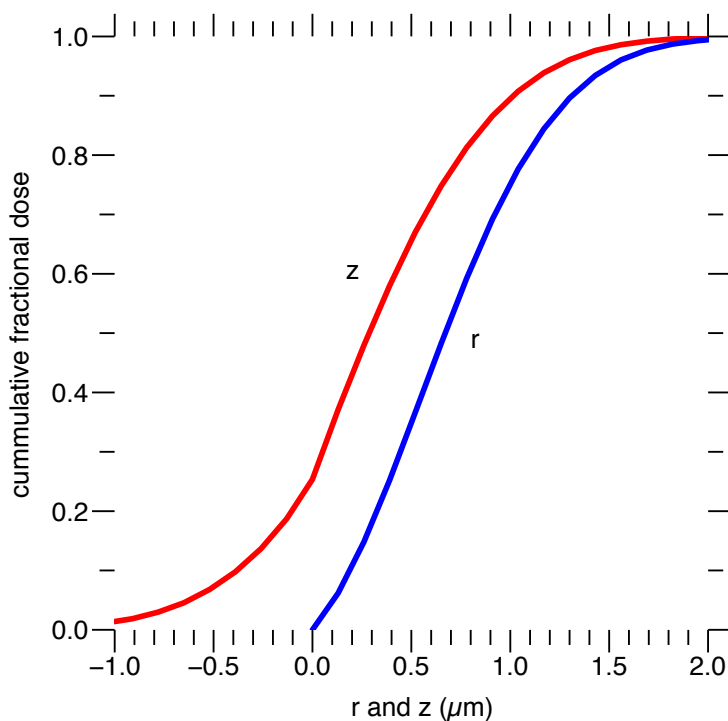

Figure 4. Cumulative dose in the axial direction (z, red) and in radial direction (r, blue) for 20 keV electrons in GaAs. The electrons are launched at r=0, z=0.
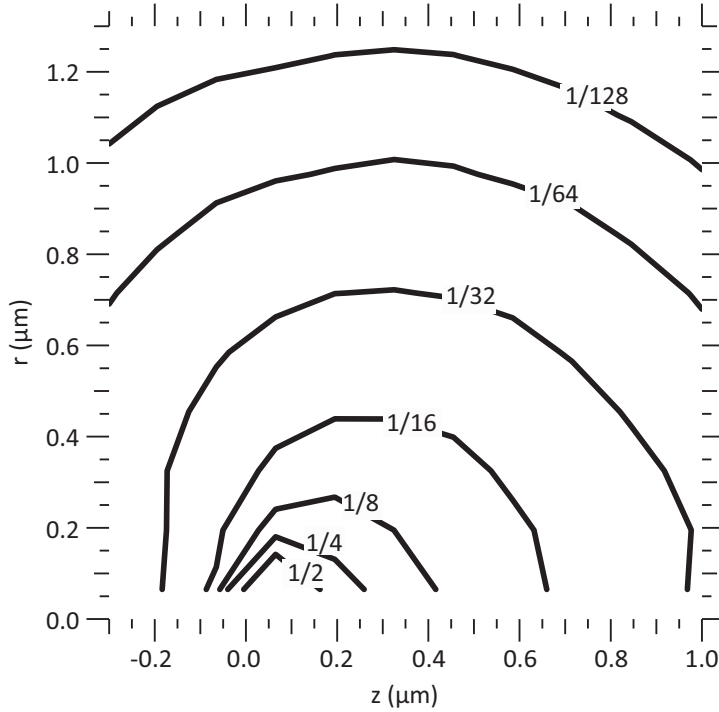
Figure 5. Electron density contours at 1 ps for 20 keV initial electrons in GaAs. Values are given relative to the peak value of 2.1×10^{16} cm^{-3}.
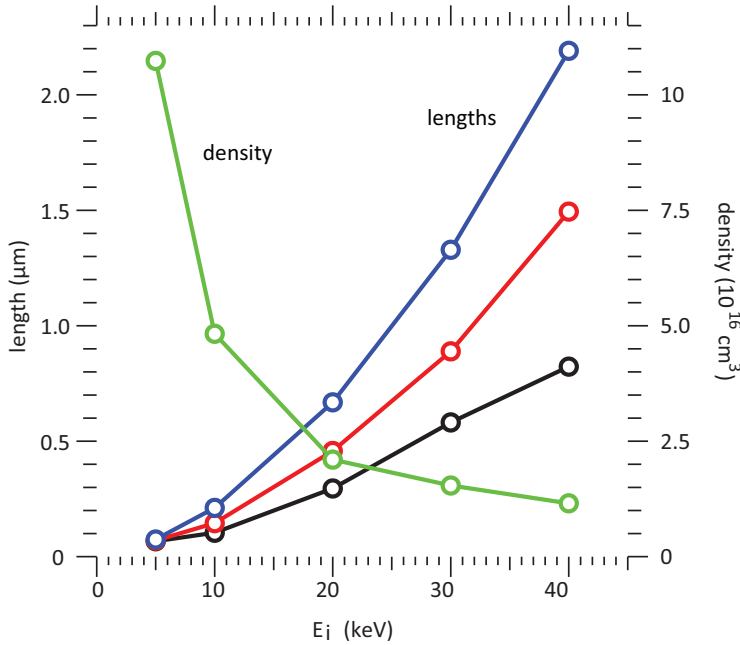
Figure 6. Characteristic lengths and peak electron density versus initial energy. The black circles indicate the distance containing ½ of the electrons behind the source ($z<0$), while the red circles give the distance containing ½ of the electrons ahead of the source ($z>0$). The blue circles gives the radius containing ½ of the electrons. The green circles show the maximum electron density on the right-hand scale.
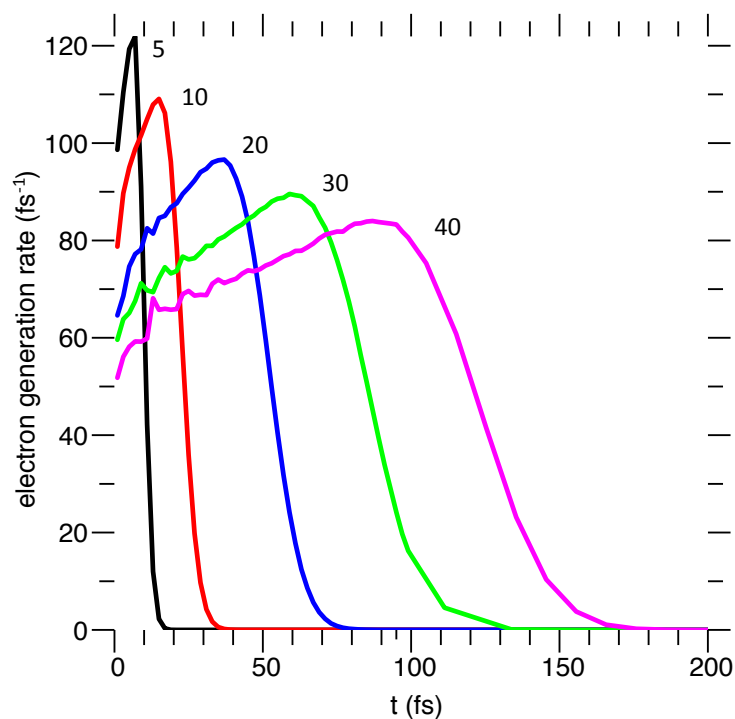
Figure 7. Electron generation rate electrons in GaAs. Initial energies range from 5 to 40 keV as indicated.
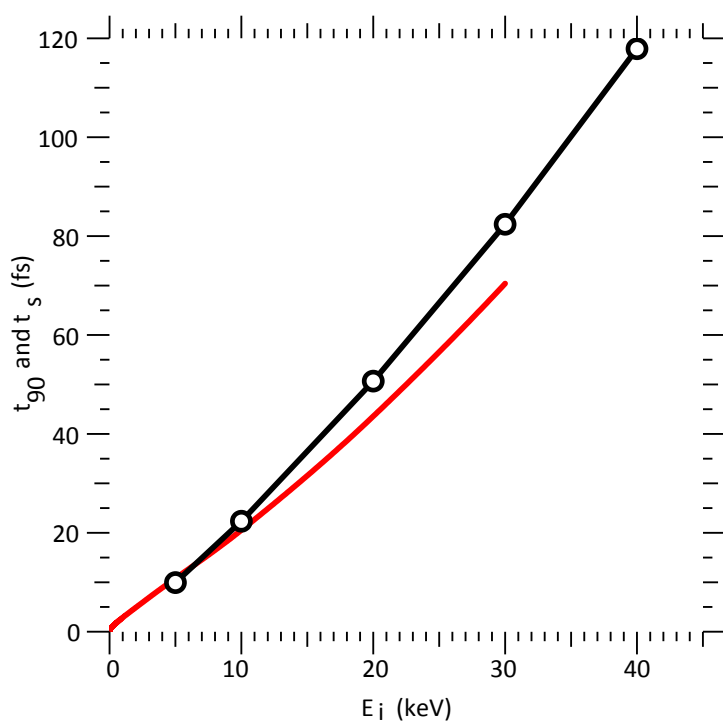

Figure 8. Electron cascade time. The Monte Carlo results for the time to create 90% of the total secondary electrons are shown by the black circles, connected by straight lines. The slowing-down time calculated from the stopping power (also shown in Figure 1) is given by the red curve.
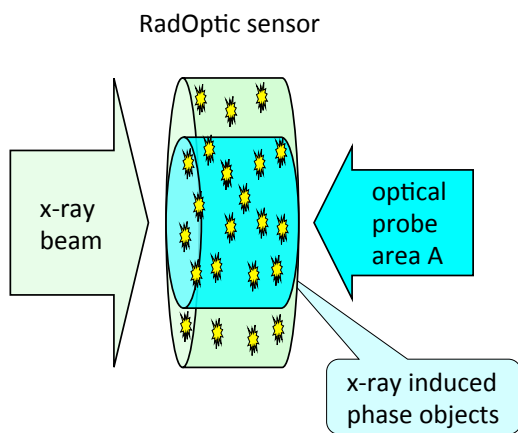
Figure A1. Interaction of the probe beam with phase objects created by the x-ray beam.